Journal of Solid State Chemistry **165,** 214–227 (2002)
doi:10.1006/jssc.2001.9490, available online at http://www.idealibrary.com on IDEAL®

Polysynthetic Twinning Characterization and Crystallographic Refinement in $NaBa_2M_2^{2+}M^{3+}O_6$ (M = Ni, Cu)

Eric Quarez, Marielle Huve, Pascal Roussel, and Olivier Mentré[1]

Laboratoire de Cristallochimie et Physicochimie du Solide de Lille, UPRESA CNRS 8012, ENSCL, BP 108, 59652 Villeneuve d'Ascq cédex, France

Received July 24, 2001; in revised form November 24, 2001; accepted December 21, 2001

Crystals of $NaBa_2M_2^{2+}M^{3+}O_6$ (M = Ni, Cu) were prepared by both electrosynthesis in molten NaOH and controlled cooling in a NaOH flux. They crystallize in an F-centered orthorhombic unit cell, space group *Fmmm*, and are formed from the stacking along c of compact $[NaM_3O_6]^{4-}$ blocks separated by Barium cations. It appears that, due to a perfect coincidence between the (a, $a\sqrt{3}$, c) unit cell constants and the related primitive hexagonal lattice (a, a, c, $\gamma = 120^\circ$), a recurrent twinning characterized by a three fold axis from one block to the subsequent one occurs in the crystals studied. Thus, the coexistence of three independent domains yields a misleading C-centered orthorhombic false symmetry. After the stacking fault detection from electron diffraction and HREM pictures a special attention was given to introduce the observed phenomenon in the X-ray data refinement process, leading to the volume ratio of three independent domains and to good reliability factors. We also investigated the composition plane located at the barium layers level. It was shown that the barium environment at the twin interface adopts a viewable oxygen coordination in agreement with the full coherence of domains boundaries observed in HREM pictures. Therefore, valence bond calculations seem to indicate a D1–D1 interface more stable than that of D1–D2 and D1–D3, comfirming the large size of superimposed monodomains. The compounds progressively decompose from 300°C, leading to a mixture of NiO, $BaCO_3$, and $BaNiO_3$. The magnetic susceptibility measured for $NaBa_2Ni_3O_6$ follows a Curie–Weiss law that involves high-spin Ni^{2+} and Ni^{3+} cations. © 2002 Elsevier Science (USA)

INTRODUCTION

The high oxidation state (+3) of copper and nickel-oxides has attracted much attention in solid state chemistry and solid state physics, notably because of the stabilization of the 3*d* orbitals that often bring their energies closer to that of the oxygen 2*p* levels. This feature gives rise to oxygen holes, rather than metal *d* electrons carriers as observed in the metallic $LaNiO_3$ and $LaCuO_3$ (1). Furthermore, the discovery of high-temperature superconducting oxides with mixed valent Cu^{II}/Cu^{III} in bidimensionnal networks has reinforced the interest. Within that framework, the synthesis and characterization of new mixed copper valence materials is justified by the necessity to provide good model compounds for Cu^{II}/Cu^{III}, coordinated to oxygens, used for instance as standards for the determination of oxidation states by X-ray absorption spectroscopy. In these materials, copper II/III exclusively adopt a square planar coordination extended to a 5- or 6-coordination by elongated apical ligands (copper Jahn–Teller effect). Several polyhedra associations such as isolated CuO_4, i.e., $Ba_4(Na,Li)CuO_4(CO_3)_2$ (2), isolated edge-sharing Cu_2O_6 dimers, i.e., $Na_6Cu_2O_6$ (3), isolated chains, i.e., $NaCuO_2$ (4) and Na_3CuO_3 (5), and infinite layers, i.e., $Ba_2Cu_3O_4Cl_2$ (6), exist. It is well known that in the high T_c superconductor $YBa_2Cu_3O_7$ (YBCO), copper adopts both the square plane coordination, CuO_4, and the pyramid ones, CuO_5 (7). In analogue materials, the nickel can adopt a more variable environment including trigonal planes, i.e., $BaNiO_2$ (8), square planes $(Li,Na)_2NiO_2$ and $K_3Ni_2O_4$ (9–11), tetrahedral, i.e., $K_9Ni_2O_7$ (12), and distorted octahedra, i.e., $BaNiO_3$ (13). Therefore, the Ni compounds rarely form edifices as observed for cuprates. From a chemical point of view, under "ordinary" conditions, trivalent copper/nickel involving the common use of high oxygen pressures or of molten alkali-hydroxide during the syntheses is unstable. Hydrothermal treatment under autogenous pressure in dilute KOH flux was recently shown to be also effective for the partial Cu^{II} to Cu^{III} oxidation in Bi_2CuO_4-related materials (14). Using barium and/or sodium peroxide as the oxidizing agent and metal oxides, Müller-Buschbaum and collaborators prepared the new $NaBa_2M_2^{2+}M^{3+}O_6$ materials (M = Cu, Ni) displaying square planar polyhedra (15,16). Those polyhedra are connected in such a way that they share their edges 6 by 6 to form original closed macro polyhedra. Single crystals of

[1]To whom correspondence should be addressed. E-mail: mentre@ensc-lille.fr.

0022-4596/02 $35.00

the copper-based materials were subsequently grown by electrosynthesis with nickel and zirconium wires for the anode and the cathode, respectively, in a KOH/NaOH mixture for the electrolyte (17). Electrochemical deposition of large $NaNiO_2$ thin single crystals (up to 3 mm) was also performed in the same study. Several attempts to prepare nonstoichiometric Na_xNiO_2 bronze by this technique led us to grow single crystals of $NaBa_2M_3O_6$ (M = Ni, Cu), which we intensively investigated by X-ray diffraction and electron microscopy from the point of view of planar faulting analysis. As a matter of fact, classical X-ray diffraction methods usually investigate an average model while HREM mainly intends to observe the real structure and is an appropriate means for investigating defects on a microscopic scale to determine their nature. The unit cell of $NaBa_2M_3O_6$ is hexagonal ($a \sim 8.31$ Å, $c \sim 11.22$ Å for the nickel compound) while its crystal structure is formed by the stacking along c of blocks which individually adopt a hexagonal symmetry. Therefore, within the stacking sequence, the sixfold axis is shifted from one layer to its surrounding homologues, involving from a global point of view the use of an orthorhombic unit cell ruled by $b = a\sqrt{3}$. This geometrical coincidence allows the appearance of twinning especially favored in the case of a perfectly coherent twin interface at the atomic level. The present work is dedicated to the complete characterization and comparison of stacking faults in the nickel phase crystals obtained by two antagonist methods. Special attention is given to clearly explain the influence of twinning on collected X-ray data, electron diffraction, and HREM pictures. Magnetic susceptibility of the prepared materials was also investigated in regard to the unusual Ni^{II}/Ni^{III} polyhedra connection within the framework.

EXPERIMENTAL

Single crystals with suitable size for X-ray characterization were synthesized by two different methods. In the first one, $NaBa_2M_2^{2+}M^{3+}O_6$ (M = Cu, Ni) crystals were grown by electrolysis of a 0.15 g CuO/NiO, 0.16 g $Ba(OH)_2$, $3H_2O$ mixture in 15 g of fused NaOH at 800°C. Nickel and zirconium foils were used as anode and cathode, respectively. Raw materials were placed in an alumina crucible, and then introduced in a quartz cell under flowing oxygen. Current versus potential scans were achieved using a TACUSSEL electronic potentiostat (Model PRT 500LG) equipped with a XY SEFRAM recorder (Model TGM 1.01). Typically, the selected working potential was chosen just at the beginning of the oxidation wave: $4\ OH^- \rightarrow O_2 + 2\ H_2O + 4e^-$, e.g., approximately 2 V. The electrodeposition was performed for a maximum of 48 h (method 1). Then electrodes were extracted from the bath and cooled to room temperature. Crystals were found indiscriminately on the nickel electrode (anode) and in the crucible. They were washed with distilled water and ethanol. Previous to our work, the method was successfully applied to several transition metal/metal experiments in order to stabilize the high oxidation state of the concerned elements, i.e., $NaNi^{3+}O_2$, $Na_xCo^{2/3+}O_2$, $Sr_{1.75}Cu_3^{2/3+}O_{5.13}$ (17), and $KBi^{5+}O_3$ (18). As already mentioned, $NaBa_2Cu_3O_6$ was also prepared this way by the same author.

Crystals of $Ba_2NaNi_3O_6$ were also obtained by controlled cooling (30°C/h) of the raw materials in sodium hydroxide flux from 750°C to room temperature (method 2). Distilled water and ethanol were used to extract NaOH and any soluble material from the cooled reaction mixture and a solid product was obtained. Attempts to prepare copper-based materials using this method failed. The products obtained by both methods tended to form black well-faceted hexagonal plates.

X-Ray powder diffraction analyses were performed on a Siemens D5000 diffractometer, with Cu$K\alpha$ radiation, using crushed single crystals. The thermal behavior of the material was investigated with a high-temperature X-ray diffraction (HTXRD) Guinier-Lenné camera with a sweeping rate of $14°C.h^{-1}$.

Magnetic data were measured with a Quantum Design MPMS-XL5 squid magnetometer. Susceptibility measurements were made in an applied field of 1 KOe upon heating from 2 to 300 K. The magnetization versus field cycle was measured at 2 K between 60 and −60 KOe.

A number of black plate-like single crystals were selected from electrochemically prepared products (method 1) as well as from cooled-in-flux preparations (method 2). Single-crystal X-Ray diffraction intensities were measured on a AXS Bruker SMART CCD-1K diffractometer under conditions shown in Table 1. For clarity reasons, results are only presented for one $Ba_2NaNi_3O_6$ single crystal (method 2) and one twinned $Ba_2NaCu_3O_6$ (method 1; the twin law is developed in the Results section). For all the selected single crystals, a total of 3×600 frames were collected (ω-scan, 10 s per frame, 0.3° oscillations for three different values of φ) at a crystal to a detector distance of 45 mm. The intensity data were then extracted from the collected frames using the program SaintPlus 6.02 (20). For each case, a Gaussian-type absorption correction (21) based on the precise crystal morphology and faces indexation was then applied using the program Xprep of the SHELXTL package (22). For an easy relationship between the hexagonal and orthorhombic unit cell, a permutation that preserves a common c axis for both trihedra was applied to the original orientation used by Müller-Buschbaum and co-workers. All the structure descriptions to come will be performed in the $a \sim 8.31$ Å, $b \sim 14.39$ Å, $c \sim 11.22$ Å unit cell. The refinements were performed using the crystallographic computing system

TABLE 1
Crystal Data, Data Collection, and Structure Refinement Parameters for a Single Crystal $Ba_2NaNi_3O_6$ and Twinned $Ba_2NaCu_3O_6$

Crystal data	M = Ni	M = Cu
Crystal symmetry	orthorhombic	orthorhombic
Space group	*Fmmm*	*Fmmm*
Unit cell refined on powder	a = 8.296(2) Å	a = 8.416(2) Å
	b = 14.369(3) Å	b = 14.577(5) Å
	c = 11.225(3) Å	c = 11.418(3) Å
Volume	1341.4(6) Å^3	1401.1(7) Å^3
Z	8	8
Calculated density	ρ = 5.64 g.cm^{-3}	ρ = 5.39 g.cm^{-3}
Data collection		
Equipment	SMART CCD	SMART CCD
Radiation Mo$K\alpha$	0.71073 Å	0.71073 Å
Scan mode	ω	ω
Recording angular range 2θ (°)	6.730–46.433	5.588–46.555
Recording reciprocal space	$-9 \le h \le 9$	$-9 \le h \le 9$
	$-15 \le k \le 15$	$-16 \le k \le 16$
	$-12 \le l \le 12$	$-12 \le l \le 12$
Number of measured ref. [$I > \sigma(I)$]	2009	3609
Nb of independant reflections [$I > 3\sigma(I)$]	278	843
Nb of independent reflections [$I > \sigma(I)$]	289	904
μ (mm^{-1}) (for $\lambda K\alpha$ = *0.71073 Å)*	19.873	19.025
Limiting faces and distances (mm)	0 1 0 0.063	0 1 0 0.032
from an arbitrary origin	0 $\bar{1}$ 0 0.057	0 $\bar{1}$ 0 0.035
	0 0 1 0.012	0 0 1 0.086
	0 0 $\bar{1}$ 0.012	0 0 $\bar{1}$ 0.087
	1 1 0 0.081	1 1 0 0.028
	$\bar{1}$ $\bar{1}$ 0 0.066	$\bar{1}$ $\bar{1}$ 0 0.032
	1 $\bar{1}$ 0 0.072	1 $\bar{1}$ 0 0.036
	$\bar{1}$ 1 0 0.079	$\bar{1}$ 1 0 0.034
Transmission factor range	0.13415–0.59804	0.13732–0.37085
R merging factor	0.0273	0.0711
Refinement parameters		
Number of refined parameters	30	32
Refinement method	Least squares on F	Least squares on F
$R_1(F)[I > 3\sigma(I)]/R_1(F)[I > \sigma(I)$	0.0193/0.0210	0.0419/0.0438
w$R2(F^2)[I > 3\sigma(I)]$/w$R2(F^2)[I > \sigma(I)]$	0.0211/0.0227	0.0448/0.0455
Weighting scheme unit		
Goof	2.02	2.79
Isotropic secondary extinction (type I) (19)	0.030(2)	0.006(2)
Max/Min $\Delta\rho$.e Å^{-3}	0.99/–0.70	1.42/–1.33

JANA 2000 (23), leading to the final reliability factors given in Table 1.

Electron diffraction patterns and high-resolution images were obtained on a Jeol 200CX and a Jeol 4000EX with a point resolution of 1.7 Å. The material was crushed and dispersed on a holey carbon film deposited on a Cu grid. The computer simulated HREM images were calculated using the multislice method and EMS program.

RESULTS AND DISCUSSION

The $NaBa_2Ni_3O_6$ crushed crystals X-ray powder pattern shows no evidence of hexagonal to orthorhombic lines splitting involving a perfect coincidence between the two networks, at the X-ray D5000 diffractometer detection limit (Fig. 1). As a matter of fact, the unit cell parameters were satisfactorily refined in the former lattice, yielding $a = 8.296(2)$ Å, $c = 11.213(2)$ Å, with the figure of merit $F(31) = 49(0.0102,62)$ [24]. The orthorhombic lattice parameters were also refined from the complete collected data sets for both nickel and copper, showing no significant deviation of the b length from its expected $a\sqrt{3}$ value. A dilatation of the unit cell from the nickel to copper materials ($a = 8.416(2)$ Å, $b = a\sqrt{3}$, $c = 11.418(3)$ Å) is observed in good agreement with the ionic radii.

The Guinier-Lenné pattern shows by the appearance of new lines that the compound begins to decompose at 300°C. The reaction is completed around 600°C (Fig. 2). After quenching in air the reaction product, the pattern shows NiO, $BaCO_3$, and $BaNiO_3$. Na may be partially present in these compounds.

Crystal Structure Description

The refined atomic coordinates and thermal parameters for the nickel and copper materials are given in Table 2. The crystal structure of $NaBa_2M_3O_6$ (M = Ni, Cu) compounds is formed by the stacking along c of two blocks related by the a and b translation and separated by barium cations within the interleaved space. Within a block, six MO_4 planar squares share their corners to form a macro hexagon parallel to (001) (Figs. 3a, 3b). They are disposed together in such a way that they share, three by three, one edge with a central NaO_6 trigonal prism. The obtained $[NaM_3O_6]^{4-}$ bidimensional pavement possesses an hexagonal symmetry with the sixfold axis running along the (0,0,z) axis and the ($\frac{1}{2}$,0,z) axis for the block centered around $z = 0$ and $z = \frac{1}{2}$, respectively (Figs. 3a,3b). The hexagonal symmetry is lost considering the two-blocks stacking. Therefore, as clearly observed in Fig. 3, it is noteworthy that the Ba(1) and Ba(2) coalescence respect both six-fold axes even if they are not rigorously located at the same z coordinate ($z_{Ba(1)} = 0.2311(1)$, $z_{Ba(2)} = \frac{1}{4}$) (Fig. 4).

As long as X-rays are concerned, for most of the investigated crystals, the first clues of the twin existence were given by the presence of a great number of intense reflections refuting the orthorhombic F Bravais lattice in

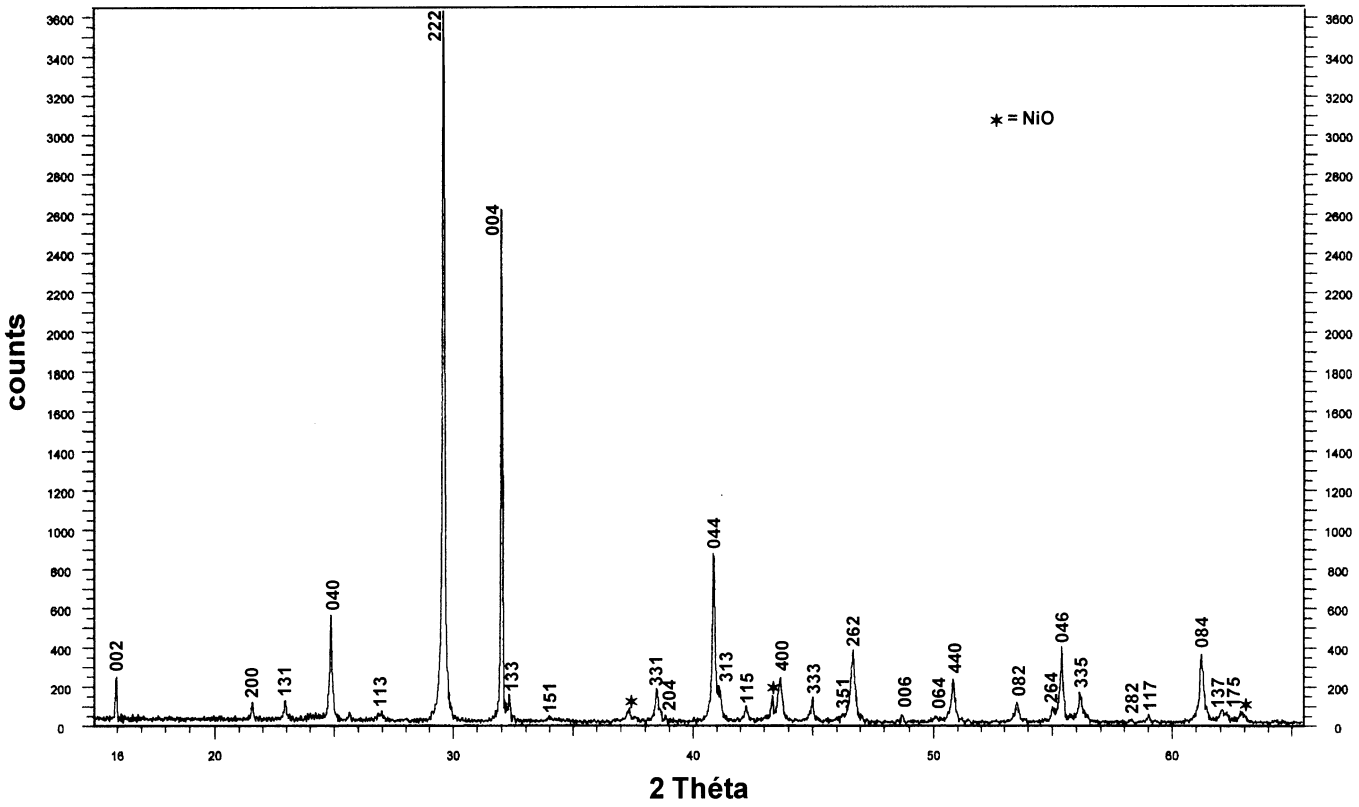

FIG. 1. X-ray powder diffraction profile of $NaBa_2Ni_3O_6$ indexed in the hexagonal lattice. It shows no split line because of the perfect orthorhombic/hexagonal unit cell coincidence.

the data set. Their existences, without refuting the previous refinement of $NaBa_2NiO_6$ in the *Fmmm* space group, question the possible modification of the crystal structure. Furthermore, all these additional reflections respect the C translations and can be taken into account in a crystal structure refinement using the *Cmmm* space group. In this last space group, the values of the reliability factors are about 8% for the several tested crystals. Nevertheless, at this stage, despite rather low *R* values, the crystal structure refinements are not fully satisfactory since they involve the splitting of the *M* cations around their special positions and the introduction of partial occupancy for a number of atoms, leading to unlikely distances in a highly disordered model. At this stage, the electronic microscopy (MET) study is largely profitable in order to distinguish between F- and C-centered crystals.

Electron Diffraction (ED) Study

[100] zone axis. We are first interested in the [100] zone, because of its easy detection. Electron diffraction patterns (EDP) of crystals exhibiting a F centering have rarely been observed (Fig. 5a). Most of them show diffuse streaks parallel to c^* (Fig. 5b), and in Figs. 5c and 5d a second system of reflections which questioned the F centering was observed. The difference between the EDP of these two last figures mainly consists of the intensity of the basic spots.

Other zone axis. The [110] EDP (Fig. 6a), obtained by the tilting of 60° around the c^* axis the [100] zone, also exhibits diffuse streaks. Additional phenomena such as extra spots refuting the F Bravais lattice and streaks were also highlighted in other zone axis patterns. The [010] and [$\bar{3}$10] patterns, deduced from each other by a rotation of 60° around c^*, are shown respectively in Figs. 6b and 6c while the [001] pattern is shown in Fig. 6d. It is noteworthy that in any case, extra spots are indexed on the basis of a C-centered unit cell, comforting single-crystal X-ray observations. In order to link these extra phenomena to a potential structure change, a high-resolution study was performed.

High Resolution Study

[100] zone axis. The modified [100] EDP of Figs. 5c and 5d are of particular interest, on one hand because of

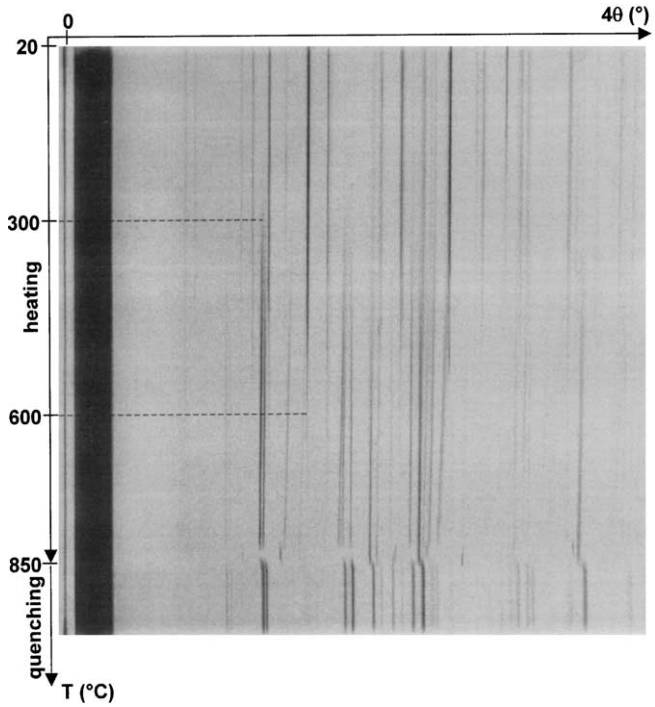

FIG. 2. High-temperature diffraction diagram (Guinnier-Lenné) for $NaBa_2Ni_3O_6$. At 300°C, the decomposition of $NaBa_2Ni_3O_6$ into NiO, $BaCO_3$, and $BaNiO_3$ starts and is completed at 600°C (see dotted lines at 300 and 600°C).

the presence of extra spots and streaks and on the other because they have often and easily been observed.

Actually, this modified [100] EDP results from the superposition of the [100] and [110] zone axis. A high-resolution image corresponding to the [100] zone axis EDP with diffuse reinforced streaks and supplementary spots (inset Fig. 7a) is shown on Fig. 7a. The coexistence of two kinds of domains randomly distributed along c and characterized by squares and triangles, respectively, is highlighted. A Fourier transform of such zones (Figs. 7b, 7c, respectively) shows that the square and triangle domains are respectively [100] and [110] orientations. The random arrangement of these domains led to the streaks along c^*. This superposition of two patterns deduced from each other by a 60° rotation around c^* is schematically represented in Figs. 8a–8c for the [100], [010], and [001] EDPs. It is perfectly coherent because of the perfect lattice hexagonal–orthorhombic coincidence. It is obvious that the ratio of square and triangle domains can vary from one crystal to another. Accordingly, the relative intensities of the basic spots of one over two rows can differ from one pattern to another (arrows in Figs. 5c and 5d), depending on the relative size of the contributing domains. An image simulation made from crystallographic data using a wide square domain, that is, a [100] zone axis, is presented in Fig. 9. A good accordance is obtained for a defocus of −280 Å and a thickness of 66 Å.

In summary the [100] orientation consists in random juxtaposition of several blocks: one majority domain [100] and another obtained by a rotation around c of 120° (in the real space). At this point it seems obvious that a third domain tilted by 240° is likely to participate. Domains turned by 120° and 240° would not be distinguishable from each other from the point of view of extra spots in the [100] and [010] EDPs. Logically, these random connections of n blocks can explain the extra phenomena observed on other zone axes.

[010] zone axis. The superposition of [010] and [$\bar{3}$10] (deduced from the [010] EDP by a 60° rotation around c^*) EDP, schematically represented in Fig. 8b, leads to the EDP of Fig. 6b (inset Fig. 10). The corresponding image

TABLE 2
Atomic Parameters and Thermal Parameters for $Ba_2NaM_3O_6$ (M = Ni (a), Cu (b))

Atom	Site	x	y	z	U_{eq}(Å^2)	U_{11}	U_{22}	U_{33}	U_{12}	U_{13}	U_{23}
Ba1 (a)	8i	0.0	0.0	0.2297(1)	0.0111(3)	0.0120(5)	0.0115(5)	0.0096(5)	0	0	0
Ba1 (b)		0.0	0.0	0.2304(1)	0.0127(6)	0.015(1)	0.013(1)	0.0104(5)	0	0	0
Ba2 (a)	8f	0.25	0.25	0.25	0.0099(2)	0.0104(5)	0.0102(5)	0.0095(4)	0	0	0
Ba2 (b)		0.25	0.25	0.25	0.0101(5)	0.012(1)	0.009(1)	0.0095(5)	0	0	0
Ni1	8g	0.6975(2)	0.0	0.0	0.0088(5)	0.011(1)	0.0098(9)	0.0055(8)	0	0	0
Cu1		0.6923(3)	0.0	0.0	0.0071(8)	0.011(2)	0.005 (1)	0.005(1)	0	0	0
Ni2	16o	0.3488(2)	0.3561(1)	0.0	0.009(4)	0.0094(7)	0.0116(7)	0.0061(6)	0.0017(5)	0	0
Cu2		0.3493(2)	0.3537(1)	0.0	0.0096(5)	0.012(1)	0.012(1)	0.0051(8)	0.0023(7)	0	0
Na (a)	8h	0.0	0.329(4)	0.0	0.011(2)	0.009(2)	0.010(2)	0.014(3)	0	0	0
Na (b)		0.0	0.3314(6)	0.0	0.016(2)	0.023(5)	0.001(4)	0.023(3)	0	0	0
					U_{iso}(Å^2)						
O1 (a)	16m	0.0	0.1845(4)	0.1128(6)	0.009(2)						
O1 (b)		0.0	0.1858(7)	0.1131(8)	0.016(2)						
O2 (a)	32p	0.2066(5)	0.4056(3)	0.8883(4)	0.012(2)						
O2 (b)		0.2075(7)	0.4059(5)	0.8889(5)	0.017(2)						

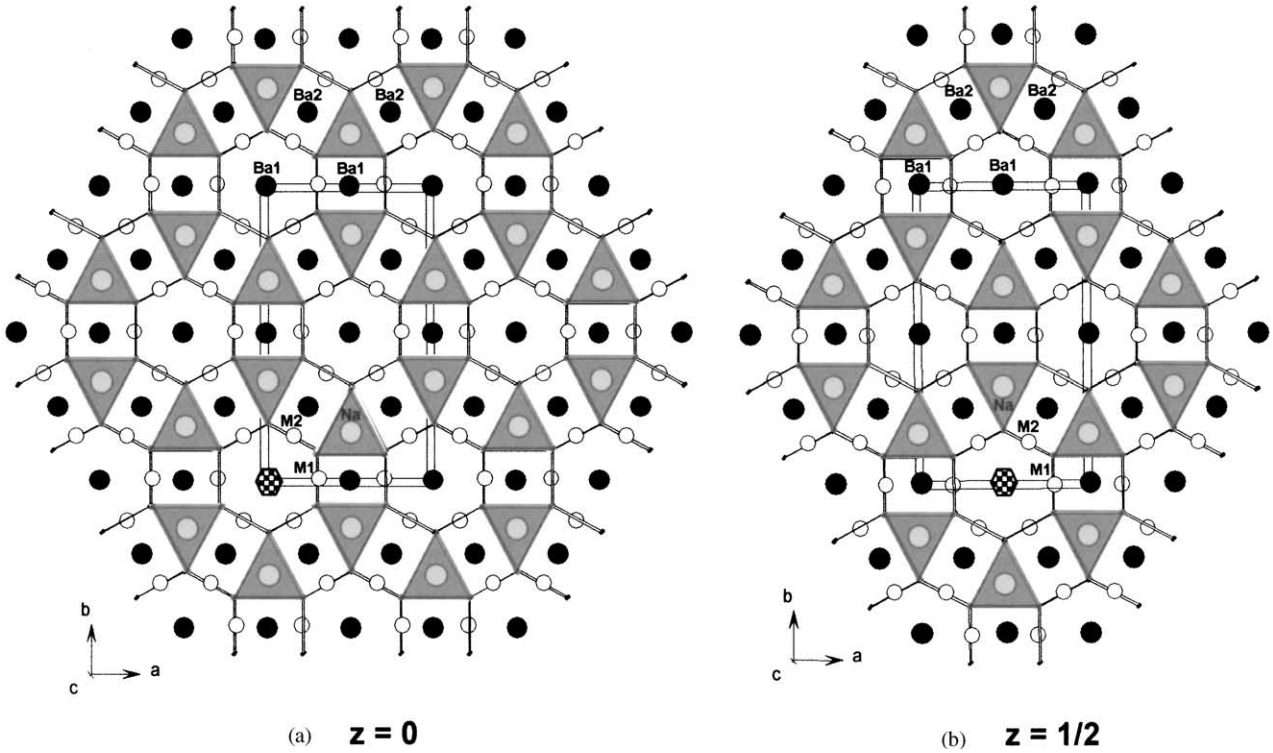

FIG. 3. Crystal structure of $NaBa_2M_3O_6$ (M = Ni, Cu). The sixfold axis of two subsequent blocks are running along (a) the (0,0,z) axis and (b) the ($\frac{1}{2}$,0,z) axis breaking the hexagonal symmetry. The barium atoms of the interleaved space are drawn in dark circles.

reveals the coexistence of two kinds of domains randomly distributed along c (Fig. 10).

[001] zone axis. The same argument can be applied to predict the look of the [001] zone axis pattern. The rotation we must apply to the [001] block to obtain the second block is always the same: 60° about the zone axis. Then the comparison of the predicted (Fig. 8c) and experimental patterns of Fig. 6d (inset Fig. 11a) points out the participation of a third domain deduced by a rotation of −60° of the first one. In other words, the [001] EDP contains three orientation variants differing by a 60° rotation about the c^* axis. Surprisingly, the corresponding image does not show any obvious sign of twinning (Fig. 11a). Actually, the observed image reflects the projection in the (a,b) plane of polydomains stacked along c. A simulated image calculated on the basis of the structural data and obtained for a thickness of 20 Å and a defocus of 300 Å is superposed on the image of the thin part of the sample (Fig. 11b). It shows that in this image only the Barium ions are highlighted. As already noted, the barium ions occupy hexagonal positions unaffected by the involved twin. That could explain why the contrast of this image, in which only the barium positions are shown, is not clearly affected by this twinning phenomenon.

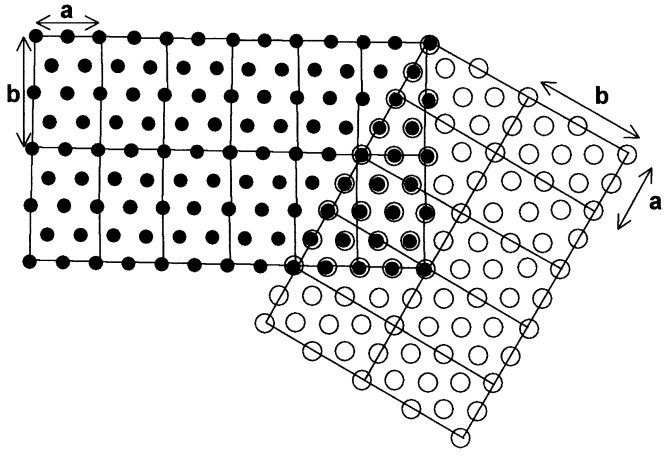

FIG. 4. Projection of Ba atoms in the (a,b) plane (black circles) and 120° rotated (white circles). The juxtaposition evidences the hexagonal symmetry of Ba atoms.

X-Ray Diffraction: Twin Refinement

The refinement of the collected data sets for seven samples were subsequently treated using the crystallographic

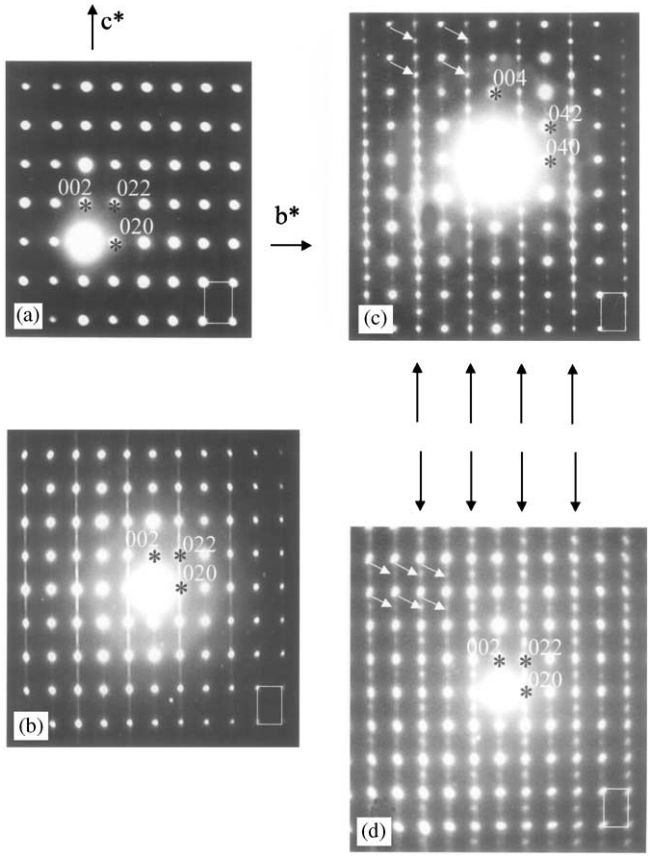

FIG. 5. [100] EDP: (a) EDP of crystals exhibiting a F symmetry, (b) most of them show diffuse streaks parallel to c^*, and (c, d) a second system of reflections (arrows) that question the F-centering lattice is observed. The contrast between the basic and extra system of reflections sets is different from that between photographs (c) and (d).

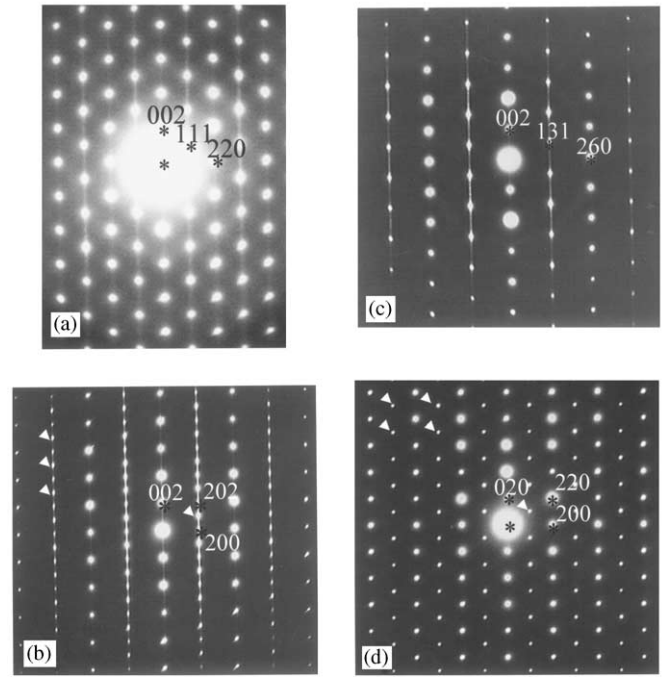

FIG. 6. Other observed zone axis patterns showing extra spots (arrows) and streaks: (a) [110], (b) [010], (c) [$\bar{3}$10], and (d) [001] zone axis patterns.

computing system JANA2000. Among the crystals studied, two with M = Cu and two with M = Ni were prepared by the electrochemical method (method 1) while three nickel samples were obtained by slow cooling in a flux (method 2); attempts to grow single crystals of the copper compound failed using this method. When necessary, twinning was taken into account during the refinement. First of all, some assumptions have been made, and consequently each twinned crystal should fulfill the following rules: (i) the crystal is composed of several *identical* domains, each domain being itself a 3-dimensional crystal; (ii) the domains are diffracting independently (i.e., there is no coherence between the different domains) and consequently, their intensities are added; (iii) boundaries effect are negligible. Most of the reflections are constituted from the overlap of several domain contributions, in agreement with the three times greater number of independent reflections reported in Table 1 for the twinned sample.

The representation of the twin operator is a twin matrix. In our case, the twin operator being a threefold axis parallel to [001], a twin law involving three domains related to each other by a 120° rotation around the c axis was introduced in the refinement process using the following *hkl* transformation matrices

$$\begin{pmatrix} h' \\ k' \\ l' \end{pmatrix}_{120°\text{rot}} = \begin{pmatrix} -\frac{1}{2} & \frac{1}{2} & 0 \\ -\frac{3}{2} & -\frac{1}{2} & 0 \\ 0 & 0 & 1 \end{pmatrix}_{T2} \begin{pmatrix} h \\ k \\ l \end{pmatrix} \quad \text{and}$$

$$\begin{pmatrix} h'' \\ k'' \\ l'' \end{pmatrix}_{240°\text{rot}} = \begin{pmatrix} -\frac{1}{2} & \frac{1}{2} & 0 \\ \frac{3}{2} & -\frac{1}{2} & 0 \\ 0 & 0 & 1 \end{pmatrix}_{T3} \begin{pmatrix} h \\ k \\ l \end{pmatrix}.$$

In this case of twinning with rational twin matrices, the data set contains groups of fully overlapped and fully separated reflections. The structure factor in the case of the complete overlapping is calculated as $F^2(H) = v_1F^2(HT_1) + v_2F^2(HT_2) + v_3F^2(HT_3)$ where v_i is the volume fraction ($v_i = V_i/\sum_i V_i$) of the ith domain and T_i, the matrix representation of the ith twinning operator. In our case, T_1 is the identity matrix, and T_2 and T_3 are the matrices written above. Note that with respect to the F-centered lattice for the *hkl* data set, $h'+k'$ ($=-2h$) and $h''+k''$ ($=h–k$) are both even numbers, according to the observed false C-centering lattice.

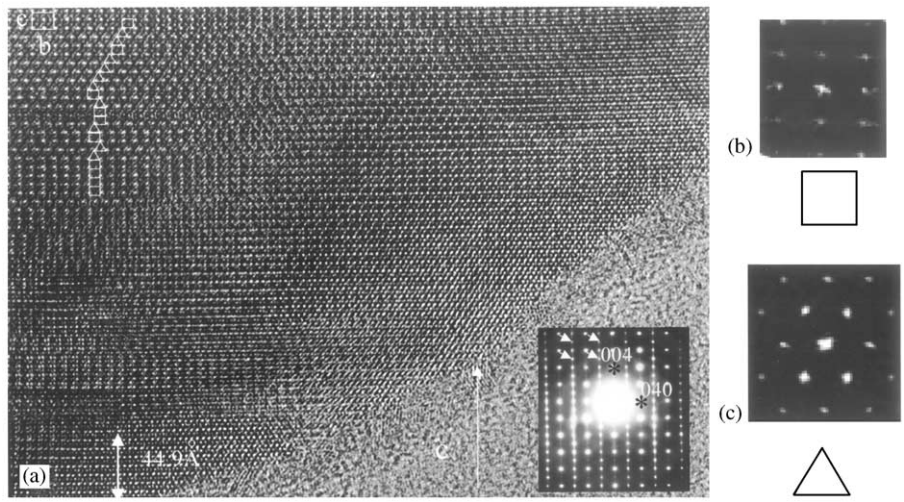

FIG. 7. (a) High-resolution image showing the coexistence of two kinds of domains randomly distributed along *c* and characterized by squares and triangles respectively. The inset corresponds to the [100] zone axis EDP with diffuse reinforced streaks and supplementary spots (arrows). A Fourier transform of such zones shows that (b) the square and (c) the triangle domains are, respectively, [100] and [110] orientations.

Thus, the volume ratio for each domain is refined using single, two, and three domains overlapped intensities. In all the treated cases, the refinement satisfactorily converged to low *R* values are listed in Table 3. It is rather instructive to examine the refined relative volume ratio of the three domains. In a first approach, crystals prepared in the flux (method 2) seem to exhibit a major domain (single domain, 58.9(4) and 66.7(8) %) while a more statistic distribution is pointed out for samples from the method 1 route (at least, two important domains except for sample 4). Even if six crystals are far from being a representative population, results may suggest that a layer-by-layer crystal growth technique (method 1) works in favor of a great concentration of a twin interface. In contrast, a more isotropic growth as performed in a flux (method 2) could generate a major central core-domain within the sample.

Selected distances deduced from the structural analysis are listed in Table 4 assorted with related valence bond sums calculated using Brese and O'Keefe data (25). For the transition metal it was calculated on the basis of both M^{2+} and M^{3+} species. Ni^{3+} and Cu^{3+}, which are not tabulated in this work, were deduced from crystal data obtained for $Ba_5Fe_2^{4+}Fe_2^{3+}Ni^{3+}O_{13.5}$ (26) with Ni in coordination six and $Ba_4NaCu^{3+}O_4(CO_3)_2$ (27), which contains square planar cations. As a matter of fact, Ba(1) and Ba(2) appear slightly underbonded and overbonded respectively, while *M*(1) and *M*(2) seem to adopt a mixed valence since the use of both M^{2+} and M^{3+} data gives intermediate results. The distances obtained for $Ba_2NaNi_3O_6$ are in good accordance with results previously reported (16). Nevertheless, it is noteworthy that the contrast between Cu(1)–O and Cu(2)–O distances announced in Ref. (15), 1.848(8) and 1.9379(2)/1.952(8) Å, respectively, is largely toned down in our study, yielding $\sim$1.87 and $\sim$1.90 Å, respectively.

In such a case that combines both a formal hexagonal lattice and an orthorhombic symmetry, it is rather instructive to describe the observed twinning within the commonly used classification from the literature. Thus, considering the Friedel formalism (28), two major classes of twinning are found according to the perfect geometrical superimposition or not from the reciprocal lattices of the antagonist twin domains. The phenomenon described here belongs to the merohedral twins type (as opposed to the pseudo-merohedral overlaps), even if the gathering of the three reciprocal lattices reduces the apparent Bravais lattice from orthorhombic F to orthorhombic C. A subgroup notation based on the twin element/crystal symmetry relation distinguishes between "purely" merohedral twins (concerning the motif; type I) and twinning by reticular merohedry (type II). This last type of twin implies the use of two different cells. In our case, which is a little bit more complex, the twin element (a threefold axis) belongs to the holohedry of the lattice (6/*m m m*), but not to the Laue class of the untwinned crystal (*m m m*). Such twins, where the crystal lattice simulates the higher symmetry of the lattice of another crystal system are due, in Friedel's terminology, to "higher order merohedry." So, the twin encountered here can be denoted as an "twin by higher order reticular merohedry" (29). An easier classification of triperiodic twins, based on the observation of the diffraction pattern, has been proposed by Donnay and Donnay (30). Here, we are dealing with a *TLS* (twinning by twin lattice symmetry) *with index n = 1* (conservation of the volume). This means that the pattern show a single

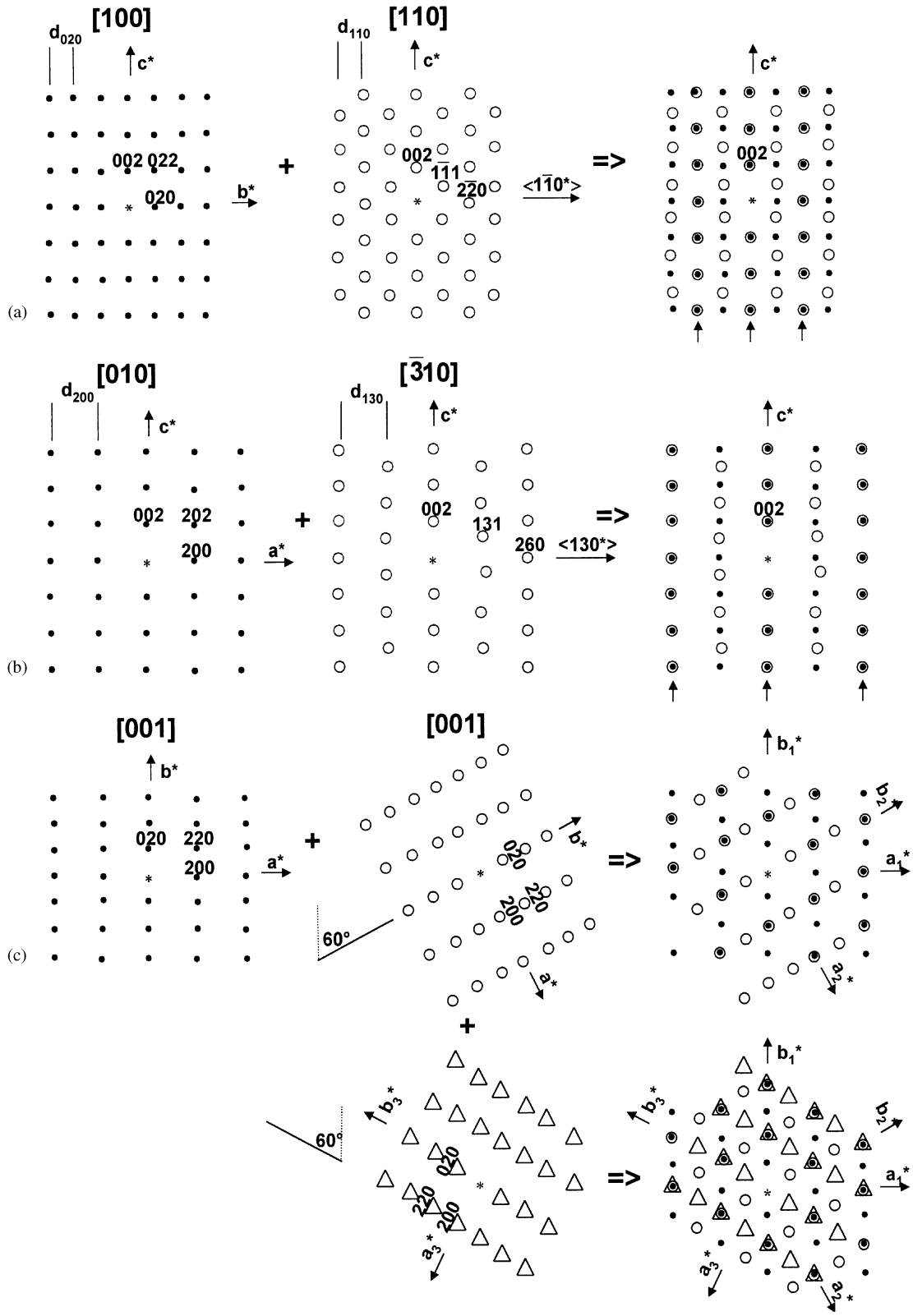

FIG. 8. Schematic representation of the superposition of the (a) [100] and [110] EDP and (b) [010] and [$\bar{3}$10] EDP. It is perfectly coherent because of the lattice hexagonal–orthorhombic coincidence. (c) The [001] and [001] EDP after a rotation of $\pm 60^\circ$ about c^*. The [001] EDP contains three orientation variants differing by a 60° rotation about the c^* axis.

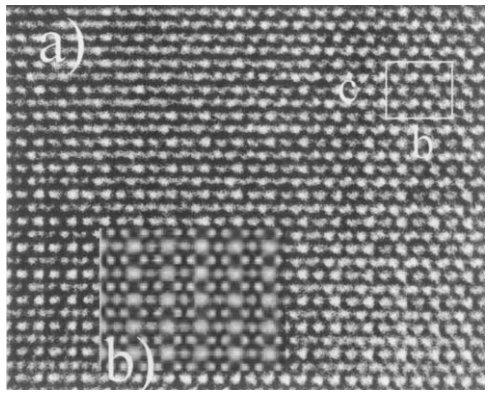

FIG. 9. (a) Enlargement of the [100] zone axis image. (b) Image simulation from crystallographic data.

orientation, with single diffraction spots (as opposed to the TLQS, twin lattice quasi-symmetry, where two or more distinct orientations of the reciprocal lattice and hence multiple diffraction spots are observed). From a morphological point of view, the twin encountered in the $NaBa_2M_2^{2+}M^{3+}O_6$ seems to be a *growth twin*, produced by accident as the crystal grows from its nucleus. It's a *rotation twin* of $2\pi/3$, the twin axis being [001]. Moreover, two components are joined in the (001) plane (known as the composition plane)—see the next section, Composition Plane. Consequently, one can label this twin as a *contact twin*. Finally, from a macroscopic point of view, we are dealing with *polysynthetic (lamellar) twinning* since the multidomain interface is repeated on a microscopic scale

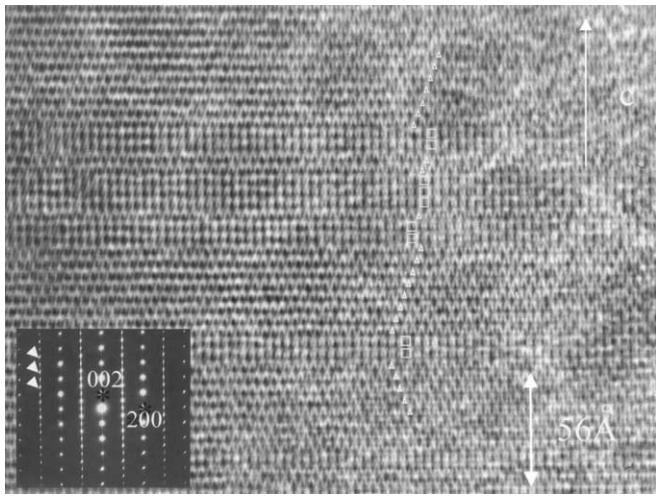

FIG. 10. (Inset) [010] and [$\bar{3}$10] EDP superposition. The arrows show the [$\bar{3}$10]-only spots, see Fig. 8b. The corresponding image reveals the coexistence of two kinds of domains randomly distributed along *c* (represented by squares and triangles).

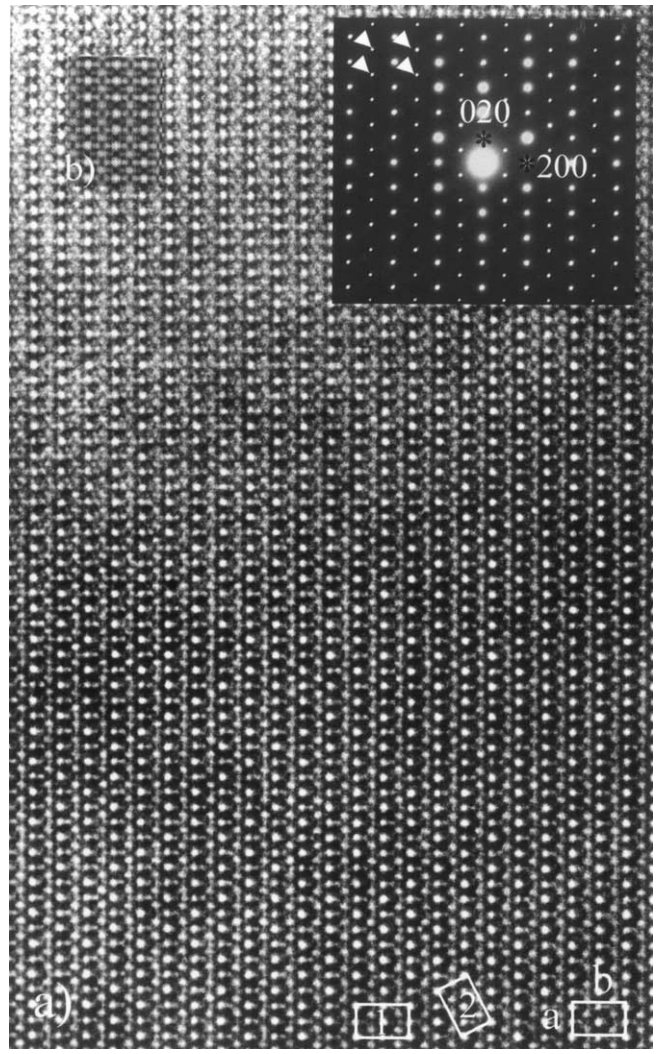

FIG. 11. The inset shows the [001] EDP containing three orientations differing by a 60° rotation about the *c** axis; supplementary spots (arrows) are the results of superposition of the three domains. (a) Corresponding image. (b) Simulated image calculated on the basis of the structural data and obtained for a thickness of 20 Å and a defocus of 300 Å.

(31) (for other examples, see $Ba_3Mo_{18}O_{28}$ (32) and $Cs_2YbNb_6Br_{18}$ (33)).

Composition Plane

Considering both the good quality of the X-ray data refinement and the HREM photographs that show the same 5.6 Å height for triangles and squares stacked along the *c* axis, a fully coherent twin interface can be deduced. Then, at the atomic scale, no drastic deviation of interface atoms environment is expected, and should lead to viewable anions–cations–anions distances at both sides of the interface as investigated in Ref. (33) for $Cs_2YbNb_6Br_{18}$.

TABLE 3
Refined Volume Ratio, Reliability Factors before and after the Twin Law Introduction, and Merging Factors for the Sudied (M = Cu, Ni) Crystals Prepared by the Two Methods

Sample	Synthesis	Deposited electrode	M	Orth. latt. parameters	R int (n ind. ref.)	$R1/R1_{twin}$	V ratio
1	Method 2	—	Ni	8.296(2) 14.369(3) 11.225(3)	2.73 (289)	1.93	No twin
2	Method 2	—	Ni	8.287(2) 14.358(4) 11.206(3)	3.94 (866)	6.31/3.03	58.9(4)/23.8(2)/17.3(2)
3	Method 2	—	Ni	8.290(11) 14.327(19) 11.238(15)	8.98 (791)	6.44/4.83	66.7(8)/16.9(5)/16.4(4)
4	Method 1	Anode	Ni	8.303(8) 14.424(13) 11.244(10)	6.46 (816)	4.37/4.02	79.8(9)/17.5(3)/2.7(2)
5	Method 1	Anode	Ni	8.320(3) 14.398(5) 11.252(4)	6.06 (893)	17.7/4.07	49.6(3)/44.7(3)/5.8(2)
6	Method 1	Anode	Cu	8.416(3) 14.577(5) 11.418(3)	7.11 (904)	10.81/4.19	42.5(4)/33.3(3)/24.2(4)
7	Method 1	Electrolyte	Cu	8.342(4) 14.502(7) 11.396(5)	7.32 (841)	14.85/4.53	42.3(4)/40.9(4)/16.8(2)
Ref. (16)	Na_2O_2 oxidation	—	Ni	8.310(8) 11.220(2) 14.397(6)	—	8.4	—
Ref. (15)	Na_2O_2 oxidation	—	Cu	8.423(2) 11.442(3) 14.406(5)	—	4.4	—

A careful examination of the crystal structure enables to deduce the accurate localization of the twin interface (the composition plane in Friedel's terminology). In the ideal structure, the [NaM_3] layers are surrounded by two oxygen layers that conserve the same sixfold axis involving an ineffective interface located at this stage. Anyway a strong modification of a Cu/Ni coordination sphere from a perfect planar square to a strongly modified polygon is unlikely and would not be stabilized. In the same way, each oxygen layer conserves the same sixfold axis as their neighboring barium sheets. Among the stacking sequence, the sixfold axis is lost beyond the barium layers at $z=\frac{1}{4}$ and $\frac{3}{4}$, so forming the ideal boundary for anti-phase domain growth. One must keep in mind that with respect to the 2-block stacking description of the structure given in the Introduction, the barium interface possesses the hexagonal symmetry toward its two surrounding blocks. So, the crystals can be described as the regular stacking of layers until a barium layer, beyond which subsequent blocks are 120°/240° rotated. Ba–O distances at the Domain1–Domain1 (D1–D1), D1–D2, and D1–D3 frontiers are shown in Fig. 12 and Table 5 with calculated valence bond sums. It appears that the Ba–O bond lengths of the Ba atoms in the ideal structure and in the twin intergrowth zone significantly deviate from one another. Therefore, at the D1–D2 interface, Ba(1) coordination splits into two Ba(1)a and Ba(1)b atoms, conserving either its $O(1)_2O(2)_4$ base on its $O(2)_4$ base. The complementary distances to oxygen ligands are four unchanged Ba–O(2) distances of 2.82 Å for the former case, and four shorter (2x Ba–O(1) and 2x Ba–O(2)) distances of 2.63 Å, leading to an overbonded Ba(1)b, $\Sigma S_{ij}=2.55$. Ba(2) shows evidence of the same kind of transformation by conserving its $(O1)_2O(2)_2$ base and splits into one almost unchanged Ba(2)a and one Ba(2)b that appears underbonded with six additional distances longer than 3 Å, $\Sigma S_{ij}=1.75$. For both cations, the same distances, and consequently the same bond valences, are obtained at the D1–D3 interface. From an electrostatic point-of-view, the monodomain formation seems favored without any high potential barium sites (2.55 for Ba(1)b), otherwise leading to unobserved zones with a completely disordered stacking sequence between thin monodomains. Therefore, the high density of defects reflects the relative stability of the interface that only perturbs one-fourth of the barium potentials in a moderate way.

TABLE 4
Selected Distances (in Å) with Related Valence Bond Sums and Angles (in°) between *M*–O–*M* for $Ba_2NaM_3O_6$ (*M* = Ni (a), Cu(b))

				ΣS_{ij}		
Ba1 (a)	–O1	2.964(7)	×2			
	–O2	3.087(4)	×4	1.74		
	–O2	2.821(4)	×4			
Ba1 (b)	–O1	3.021(11)	×2			
	–O2	3.130(6)	×4	1.54		
	–O2	2.865(6)	×4			
Ba2 (a)	–O1	2.75(4)	×4	2.3		
	–O2	2.75(4)	×4			
Ba2 (b)	–O1	2.783(6)	×4	2.08		
	–O2	2.794(7)	×4			
Ni1	–O2	1.851(4)	×4	Ni^{2+} 2.35	Ni^{3+} 2.64	
Cu1	–O2	1.873(7)	×4	Cu^{2+} 2.37	Cu^{3+} 2.82	
Ni2	–O1	1.876(5)	×2	Ni^{2+} 2.23	Ni^{3+} 2.52	
	–O2	1.863(4)	×2			
Cu2	–O1	1.899(7)	×2	Cu^{2+} 2.20	Cu^{3+} 2.62	
	–O2	1.901(7)	×2			
Na (a)	–O1	2.436(8)	×2	1.16		
	–O2	2.393(5)	×4			
Na (b)	–O1	2.484(13)	×2	1.07		
	–O2	2.416(7)	×4			
Ni1	–Ni2	2.423(2)				
Ni2	–Ni2	2.509(2)				
Cu1	–Cu2	2.509(2)				
Cu2	–Cu2	2.537(3)				
Ni1–O2–Ni2		81.4(2)				
Ni2–O1–Ni2		83.9 (2)				
Cu1–O2–Cu2		83.3(2)				
Cu2–O1–Cu2		83.8(4)				

Magnetic Properties

Far from the twin preoccupation, but in regard to the unusual *M* network, the magnetic susceptibility of the nickel compound was investigated. The thermal evolution of χ and χ^{-1} is shown in Fig. 13. It is characteristic of an antiferromagnetic ordering with $T_N = 5$ K. A Curie–Weiss law is observed from 300 to 120 K ($p_{eff} = 6.31\ \mu B$/f.u., $\theta_c = -447$ K), the temperature below which χ^{-1} becomes concave upward, a sign of the progressive settings of magnetic interactions due to the bidimensional character of the layers being magnetically isolated. The measured p_{eff} value involves high-spin cations and an efficient orbital splitting due to the planar-square crystal field. Thus, the higher spin configuration viewable in this case would be 2 Ni^{2+}: $(d_{xz},d_{yz})^4\ d^2_{xy}\ d^1_{(z^2)}\ d^1_{(x^2-y^2)}$ and 1 Ni^{3+}: $(d_{xz},d_{yz})^4\ d^1_{xy}\ d^1_{(z^2)}\ d^1_{(x^2-y^2)}$ per formula unit, yielding $p_{eff} = 5.56\ \mu B$/f.u in a spin-only configuration. Even such a model involves spin–orbit coupling influence to explain the experimental data. The magnetization cycle versus applied field measured at 2 K is linear, refuting any residual moment. Considering the M^{2+}/M^{3+} network, it is rather complicated to predict the engaged couplings. Within the macro-hexagon *M*–*M* distances are rather short (closed to 2.5 Å) but the orbitals are pointing toward oxygen with M–O–M angles closed to 90°. Thus, both superexchange and double exchange are in competition. The *M*–*M* interhexagon distances are closed to 3.3 Å and would be active through direct exchanges via possible d_{z^2}, d_{yz}, and d_{xz} orbitals. The magnetic structure should be very interesting to investigate to quantify accurately the engaged couplings.

TABLE 5
Ba–O Distances at Domain 1–Domain 1 (D1–D1), D1–D2 and D1–D3 with Calculated Valence Bond Sums (ΣS_{ij})

No rotation						120° rotation						240° rotation					
					ΣS_{ij}						ΣS_{ij}						ΣS_{ij}
Ba1	–O1	2.964(7)	×2	D1	1.74	Ba1a	–O1	2.96	×2	D1	1.74	Bala	–O1	2.96	×2	D1	1.74
	–O2	3.087(4)	×4				–O2	3.09	×4				–O2	3.09	×4		
	–O2	2.821(4)	×4	D1			–O2	2.82	×4	D2			–O2	2.82	×4	D3	
						Ba1b	–O2	2.82	×4	D1	2.55	Bala	–O2	2.82	×4	D1	2.55
							–O1	2.63	×2	D2			–O1	2.63	×2	D3	
							–O2	2.62	×2				–O2	2.62	×2		
Ba2	–O1	2.750(4)	×2	D1	2.31	Ba2a	–O1	2.75	×2	D1	1.75	Ba2a	–O1	2.75	×2	D1	2.31
	–O2	2.750(4)	×2				–O2	2.75	×2				–O2	2.75	×2		
	–O1	2.750(4)	×2	D1			–O1	3.07	×2	D2			–O1	2.75	×2	D3	
	–O2	2.750(4)	×2				–O2	3.19	×2				–O2	2.75	×2		
							–O2	3.20	×2								
						Ba2b	–O1	2.75	×2	D1	2.31	Ba2b	–O1	2.75	×2	D1	1.75
							–O2	2.75	×2				–O2	2.75	×2		
							–O1	2.75	×2	D2			–O1	3.07	×2	D3	
							–O2	2.75	×2				–O2	3.19	×2		
													–O2	3.20	×2		

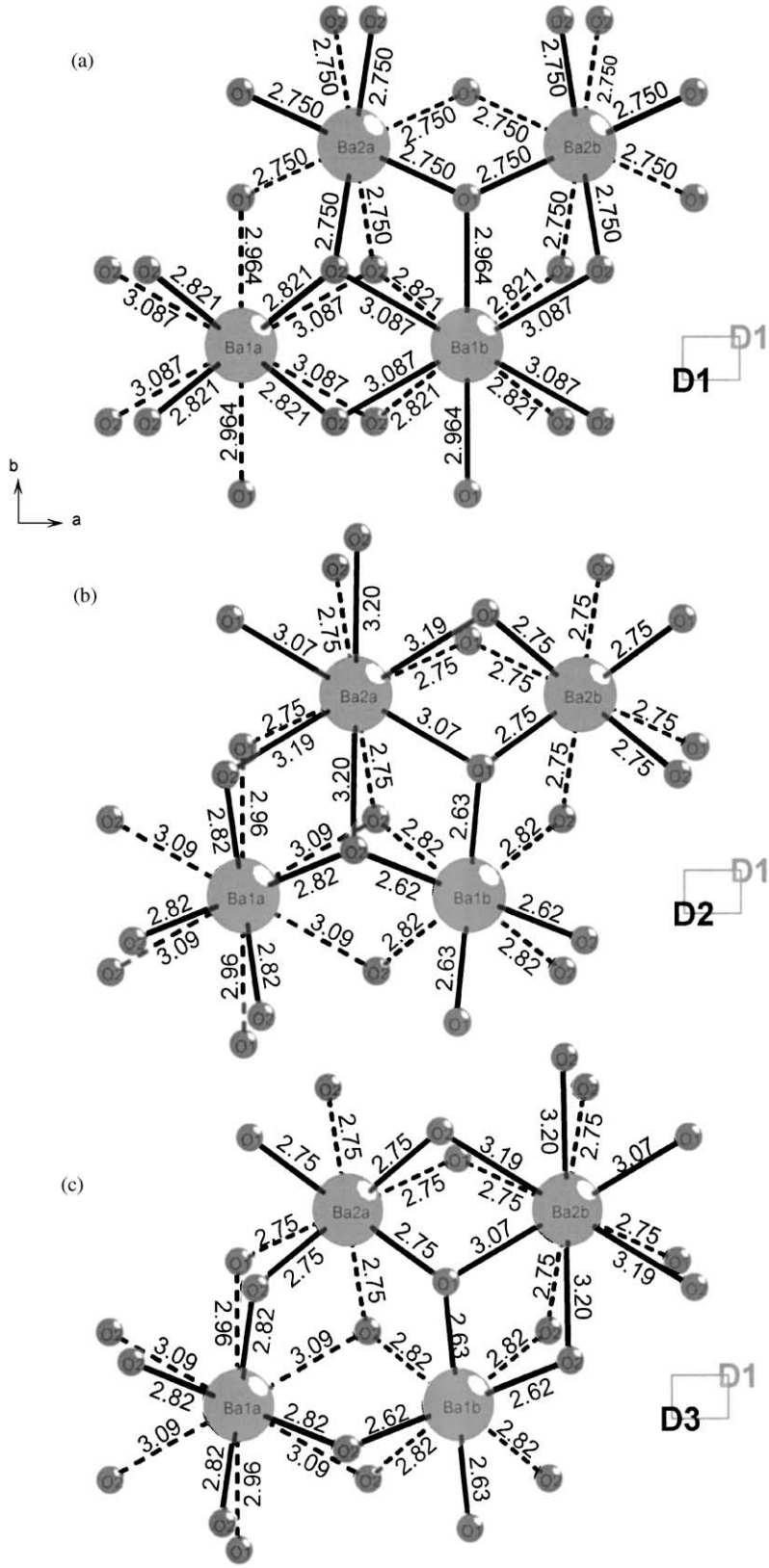

FIG. 12. Ba environment at the twin interface. (a) monodomain, (b) D1 (broken line distances)–D2 (120° rotation) interface, and (c) D1–D3 (240° rotation interface).

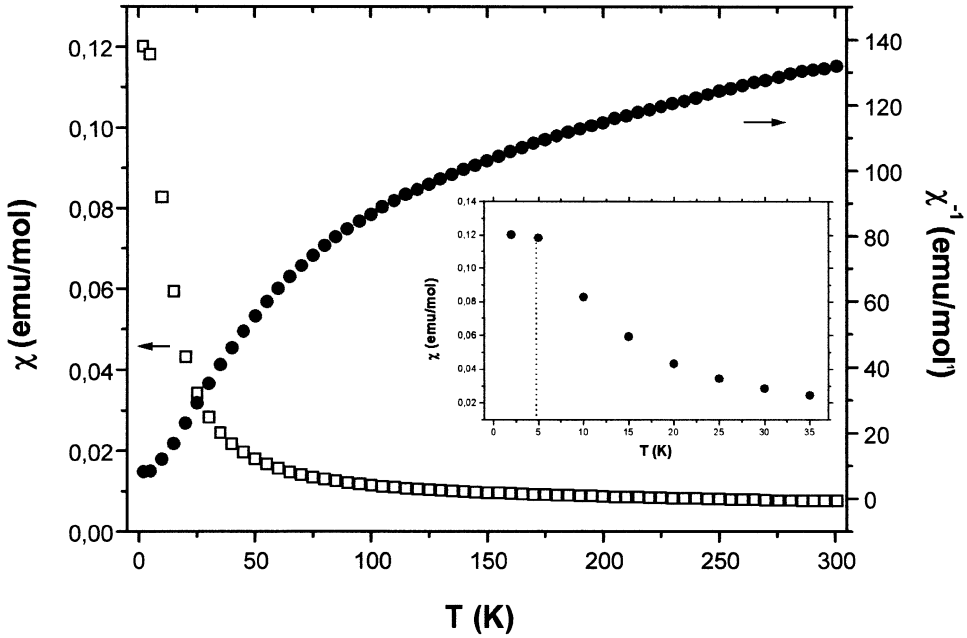

FIG. 13. Temperature dependence of magnetic susceptibility and its inverse for $NaBa_2Ni_3O_6$. The inset highlights the low-temperature behavior.

ACKNOWLEDGMENTS

The authors sincerely thank Professor F. Abraham (LCPS), Professor G. Van Tendeloo for useful discussions, and the EMAT laboratory (Antwerp, Belgium) for microscopy facilities.

REFERENCES

1. J. Zaanen, G. A. Sawatzky, and J. W. Allen, *Phys. Rev. Lett.* **55,** 418 (1985).
2. H. A. Weakliem, K. Guda, B. Corona, and D. S. McClure, *J. Solid State Chem.* **119,** 359 (1995).
3. N. Bukovec, J. Leban, and R. Hoppe, Z. *Anorg. Allg. Chem.* **563,** 79 (1988).
4. K. Hestermann and R. Hoppe, *Z. Anorg. Allg. Chem.* **367,** 261 (1969).
5. K. Hestermann and R. Hoppe, *Z. Anorg. Allg. Chem.* **367,** 270 (1969).
6. Hk. Müller-Buschbaum, *Angew. Chem. (Int. Ed. Engl.)* **30,** 723 (1991).
7. J. J. Capponi, C. Chaillout, A. W. Hewat, P. Lejay, M. Marezio, N. Nguyen, B. Raveau, J. L. Soubeyroux, and J. L. Tholence, *Europhys. Lett.* **3,** 1301 (1987).
8. J. J. Lander, *Acta Crystallogr.* **4,** 148 (1951).
9. H. Rieck and R. Hoppe, *Z. Anorg. Allg. Chem.* **392,** 193 (1972).
10. H. Zentgraf and R. Hoppe, *Z. Anorg. Allg. Chem.* **462,** 71 (1980).
11. H. Zentgraf K. Claes, and R. Hoppe, *Z. Anorg. Allg. Chem.* **462,** 92 (1980).
12. H. Zentgraf and R. Hoppe, *Z. Anorg. Allg. Chem.* **462,** 80 (1980).
13. Y. Takeda, F. Kanamaru, M.Shimada, and M. Koizumi, *Acta Crystallogr. Sect.* **B 32,** 2464 (1976).
14. N. Henry, O. Mentré, J. C. Boivin, and F. Abraham, *Chem. Mater.* **13,** 543 (2001).
15. G. Tams and Hk. Müller-Buschbaum, *Z. Anorg. Allg. Chem.* **617,** 19 (1992).
16. M. Strunk and Hk. Müller-Buschbaum, *Z. Anorg. Allg. Chem.* **619,** 343 (1993).
17. T. N. Nguyen, Ph.D. dissertation. Massachusetts Institute of Technology, 1994.
18. T. N. Nguyen, D. M. Giaquinta, W. M. Davis, and H.-C. zur Loye, *Chem. Mater.* **5,** 1273 (1993).
19. P. J. Becker and P. Coppens, *Acta Crystallogr. Sect. A* **30,** 129 (1974).
20. SAINT + ver. 5.00, Bruker Analytical X-Ray Systems, 1998.
21. W. R. Busing and H. A. Levy, *Acta Crystallogr.* Sect. *A* **10,** 180 (1957).
22. G. M. Sheldrick, SHELXTL NT ver. 5.1, Bruker Analytical X-Ray Systems, 1998.
23. V. Petricek and M. Dusek, JANA 2000. Institute of Physics, Praha, Czech Republic, 1997.
24. G. S. Smith and R. L. Snyder, *J. Appl. Cryst.* **12,** 60 (1979).
25. N. E. Brese and M. O' Keefe, *Acta Crystallogr. Sect. B* **47,** 192 (1991).
26. H. Takizawa and H. Steinfink, *J. Solid State Chem.* **121,** 133 (1996).
27. P. D. Vernooy and A. M. Stacy, *J. Solid State Chem.* **95,** 270 (1991).
28. G. Friedel, "Leçons de Cristallographie." Ed. Berger-Levrault, Paris, 1926.
29. V. J. Hurst, J. D. H. Donnay, and G. Donnay, *Miner. Mag.* **31,** 145 (1956).
30. G. Donnay and J. D. H. Donnay, *Can. Mineral.* **12,** 422 (1974).
31. C. Giacovazzo, H. L. Monaco, D. Viterbo, F. Scordari, G. Gilli, G. Zanetti, and M. Catti, "Fundamentals of Crytallography" (C. Giacozzo, Ed.) International Union of Crystallography Texts on Crystallography 2. Oxford Univ. Press, New York, 1992.
32. R. Ramlau, R. E. McCarley, and A. Simon, *J. Solid State Chem.* **142,** 89 (1999).
33. R. Ramlau, V. Duppel, A. Simon, S. Cordier, C. Perrin, and M. Sergent, *J. Solid State Chem.* **141,** 140 (1998).